Science Advances

AAAS

Supplementary Materials for

Bioinspired two-in-one nanotransistor sensor for the simultaneous measurements of electrical and mechanical cellular responses

Hongyan Gao *et al.*

Corresponding author: Jun Yao, juny@umass.edu

The PDF file includes:

Figs. S1 to S23
Tables S1 and S2
Legends for movies S1 and S2
References

Other Supplementary Material for this manuscript includes the following:
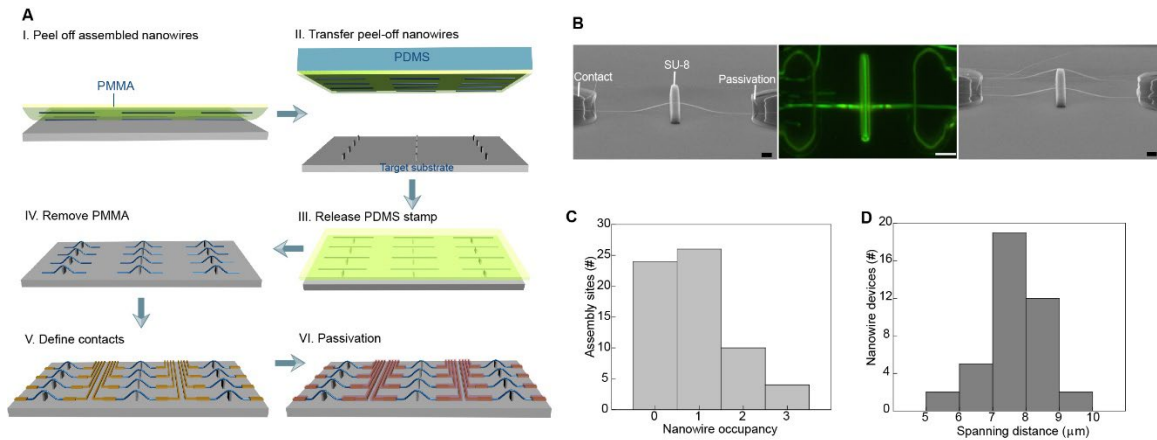
Movies S1 and S2

Fig. S1. 3D nanotransistor fabrication. (**A**) Schematic flow of the nanowire assembly and device fabrication process. The details of the assembly can be found in Ref. 1. Briefly, planar Si nanowire arrays were first assembled by a deterministic 'combing' technique (*25, 28*) on a Si substrate (covered with 600 nm SiO₂). A thin layer of poly(methyl methacrylate) (PMMA, Microchem 950 C2) with the thickness of ~100 nm was spin-coated onto the assembled nanowires, which was then peeled off using water intercalation (*25*) to carry the embedded nanowires (step-I). A soft stamp (~1 mm thick) made from polydimethylsiloxane (PDMS, Sylgard 184, 10:1) was used to pick up the peeled-off PMMA layer and transferred onto a Si substrate with predefined SU-8 (Microchem 2002) microbar arrays (height ~1.4 μm) defined by electron beam lithography (step-II). The PMMA layer was release from the PDMS stamp (step-III), assisted by a thermal treatment (100 °C, 2 min). The PMMA layer was dissolved in acetone, leaving the nanowires on the microbars to form the 3D structures (step-IV). Electrical contacts (Cr/Pd, 3/70 nm) were subsequently defined by using standard photolithography, metal evaporation, and lift-off processes (step-V). The contacts and interconnects were further passivated with a Si₃N₄ layer (~90 nm) to prevent current leakage in solution (step-VI). (**B**) Representative scanning electron microscope (SEM) images of fabricated single-wire (left) and double-wire (right) 3D nanotransistors. Scale bars, 1 μm. The middle panel shows a top-view optical (dark-field) image of the nanotransistor same as shown in the left panel. Scale bar, 2 μm. (**C**) Statistics showed that (40.6%) of the assembled sites were single-wire structures, 15.6 % were double-wire structures, and 6.2 % were triple-wire structures. The result was consistent with previous report (*25*). Given that multi-wire device is still able to detect signals at cellular resolution, it led to a total device yield ~63%. (**D**) Statistics of the spanning distance in assembled nanowire structures, showing a value of 7.8 ± 0.9 μm.
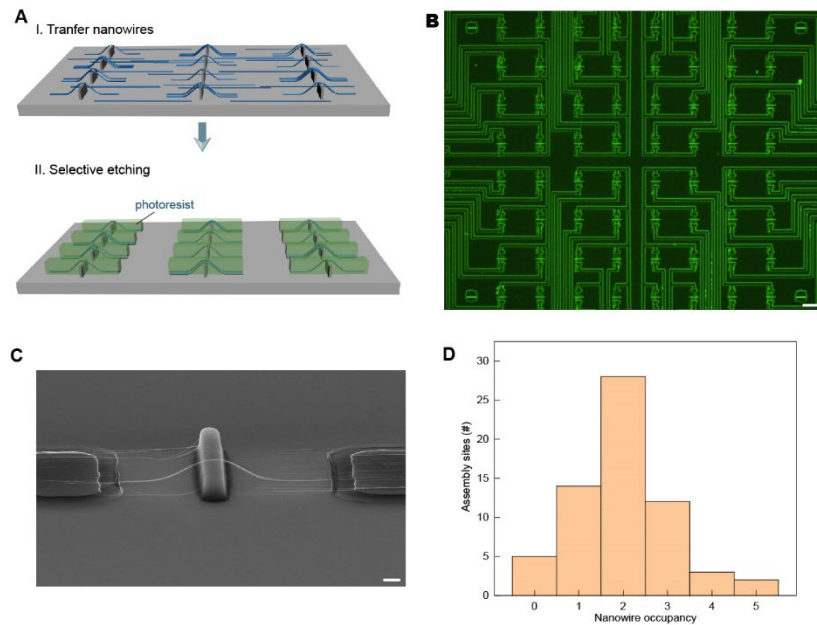
Fig. S2. 3D nanotransistor fabrication-II. (**A**) Schematic of an alternative 3D assembly. The nanowires were initially aligned randomly across the entire substrate using a contact printing method (*60*). Then they were peeled off and transferred onto pre-defined SU-8 microbar arrays (top panel) following the standard procedures described in Fig. S1A. Arrays of photoresist stripes (Microchem LOR 5A + S1805) were then lithographically patterned at the assembly sites to serve as protective masks (bottom panel). Nanowires outside the mask region were etched by reactive ion etch ($SF_6/O_2 = 20/50$ sccm; 100 W, 30s), with the photoresist subsequently dissolved (PG remover, Microchem). (**B**) Dark-field optical image of a fabricated matrix of 8 × 8 nanotransistors using this strategy. Scale bar, 50 μm. (**C**) SEM image of a representative device from the device arrays. Scale bar, 1μm. (**D**) Statistics showed that ~93% of the assembled sites had nanowires.
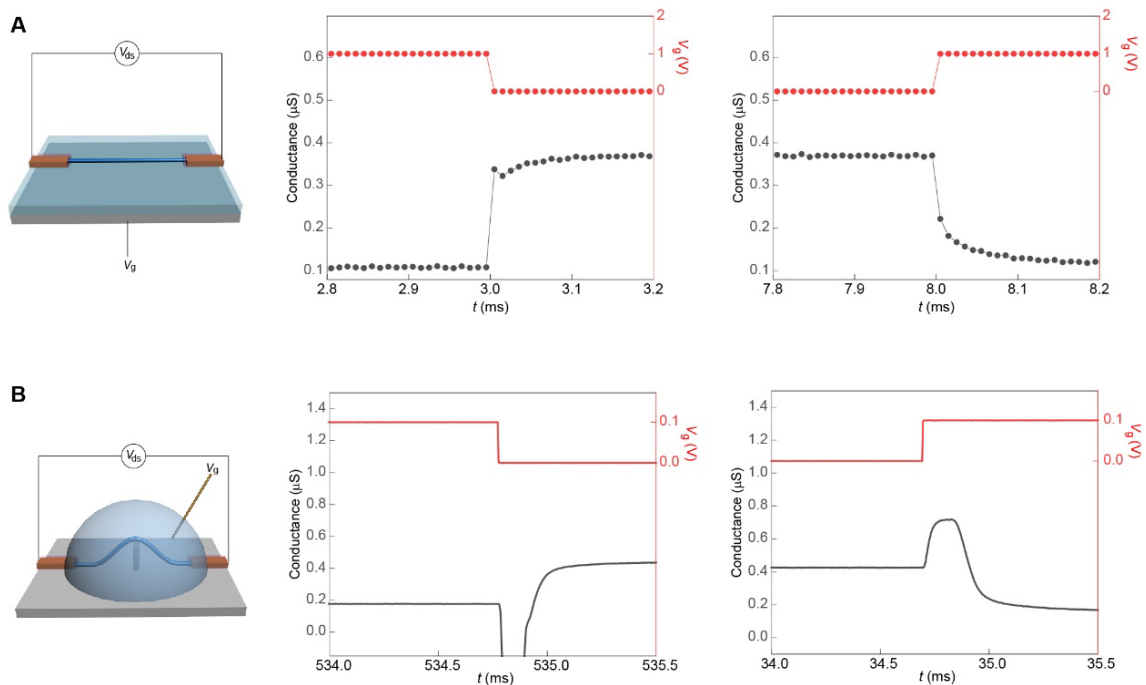
Fig. S3. Temporal dynamics in Si nanowire devices. (A) (Left) The intrinsic response time in the Si nanowire was tested using a back-gate transistor configuration (*e.g.*, using the Si substrate as back gate across 600 nm SiO_2). The transistor was biased with a constant source-drain voltage V_{ds}=0.1V. (Middle and right) Step gate voltages of 1→0 and 0→1V (red curves) were applied to the back gate with the conductance change monitored. Both the rising and falling time in the conductance response were ⩽10 μs (black curves). Note that the recording was limited to a sampling frequency of 100 kHz to resolve faster dynamics. (B) (Left) The temporal response of the nanowire transistor was measured in physiological solution. The transistor was biased with a constant source-drain voltage V_{ds}=0.1V. (Middle and right) Step gate voltages of 0.1→0 and 0→0.1V (red curves) were applied to the water gate with the conductance change monitored. Surging spikes of ~0.18 ms and ~0.29 ms were observed during the transitions (black curves). These surging spikes and their temporal features were consistent with other work studying Si-nanowire response in solution environment (*43*). The spikes were attributed to the extrinsic capacitive effect in the extending (*e.g.*, cm length) passivated metal interconnects (*43*). Localized cellular membrane potential shall not induce appreciable capacitive effect. The temporal feature (*e.g.*, signal width) is still considerably faster than the action potential measured (*e.g.*, > 5 ms).
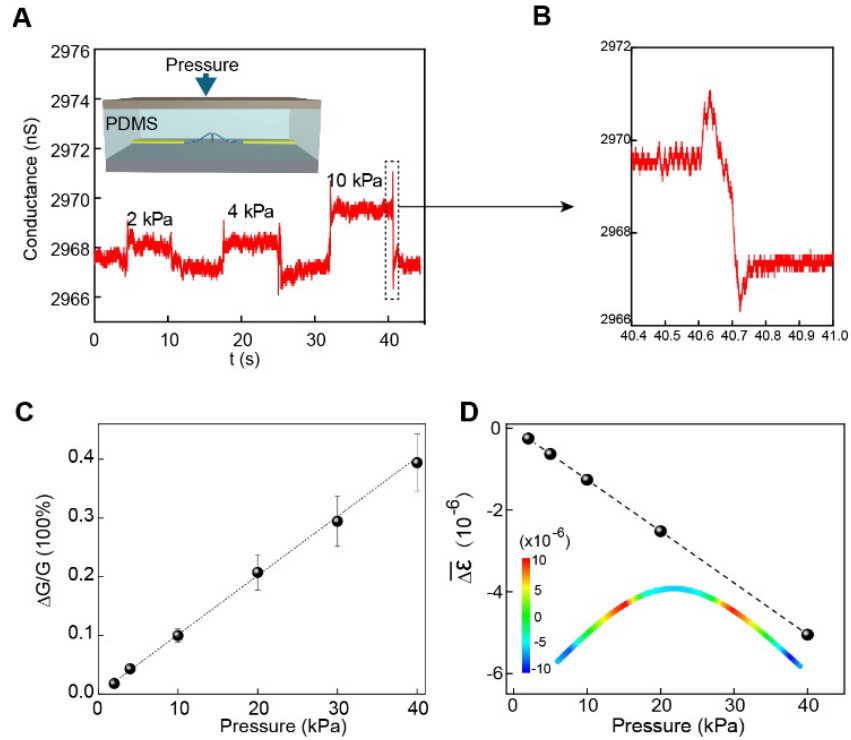
Fig. S4. Mechanical testing and simulation of nanotransistors. (**A**) Conductance change in a nanotransistor with respect to the pressure applied on it through a layer of PDMS elastomer (280 μm thick). (**B**) Zoom-in feature of the possible artifact signal induced during mechanical loading, which may have come from capacitive charge effect at the PDMS-device interface (*e.g.*, possible triboelectric effect due to the microporous feature in PDMS). The temporal dynamics in the artifact (~100 ms) is completely different from recorded cellular signals (~1.2 s in Fig. 2C and ~20 ms in Fig. 2D). The absence of artifact signal during cell recording is expected from two possible reasons: 1) cell-device has an intimate interface (fig. S7); 2) the ionic solution environment facilitates charge dissipation and further depresses mechanical artifact. (**C**) Average relative conductance change, $\Delta G/G$, with respect to applied pressure P from 6 devices. This plot is same as Fig. 1H. (**D**) Net strain $\Delta\varepsilon$ in the nanowire with respect to applied pressure P from simulation. The negative sign indicates a compressive strain. For simulation (by finite element analysis using Abaqus/Standard (2020)), the nanotransistor was placed at the central region of a PDMS matrix ($20 \times 20 \times 2$ μm^3, $W \times L \times H$) with uniform pressure applied from the top. The elastic modulus of the SU-8, PDMS, and Si nanowire was taken as 2.0 GPa, 2.6 MPa, and 188 GPa, respectively (*27, 61*).

From (C), the average slope or conductance change per kP, is $k1 = (\frac{\Delta G}{G})/P = (9.6 \pm 1.3) \times 10^{-5} \text{kPa}^{-1}$. From (D), the slope or net strain $\Delta\varepsilon$ per kP, is $k2 = \Delta\varepsilon/P = -1.26 \times 10^{-7} \text{ kPa}^{-1}$. Therefore, the average gauge factor (*24*) is $g = \frac{(\frac{\Delta R}{R})}{\Delta\varepsilon} = -\frac{(\frac{\Delta G}{G})}{\Delta\varepsilon} = -\frac{k1}{k2} = (7.6 \pm 1.0) \times 10^2$. For a resolvable pressure of 2 kPa (A) with corresponding strain of -2.5×10^{-7} (C), the equivalent force exerted along the nanowire axis is $F = E \times \Delta\varepsilon \times (\frac{\pi d^2}{4}) = 33$ pN, where E, d correspond to elastic modulus (188 GPa) and diameter (30 nm) of Si nanowire, respectively.
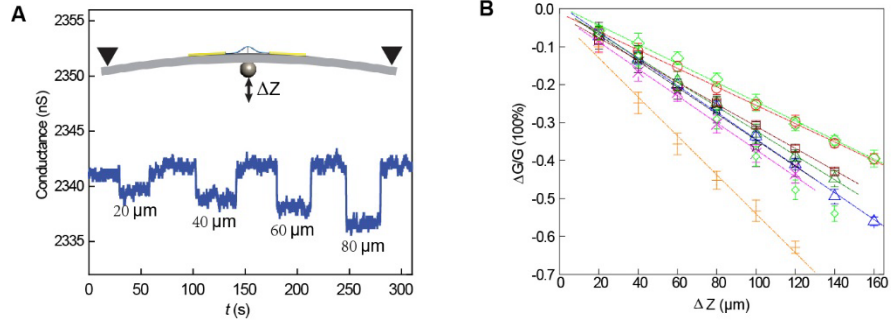
Fig. S5. Tensile-strain response in nanotransistors. (**A**) (Inset) Schematic setup for bending the nanotransistor. Specifically, the devices were fabricated on the central region of a rectangular Si substrate (4 cm × 7 cm). Both the lateral edges (along the width) of the substrate were mechanically fixed. A sapphire bead (3 mm diameter) was placed beneath of the substrate center and displaced by a micrometer in the vertical direction to bend the substrate. A decrease in conductance was observed with the increase in the vertical displacement, ΔZ. (**B**) Conductance change with respect to ΔZ in devices ($N = 9$), showing a linear relationship. The average slope was $-(3.5 \pm 0.76) \times 10^{-3}$ μm^{-1}. The linear decrease in conductance at increasing tensile strain was consistent with test results in fig. S4, where compressive strain yielded conductance increase.
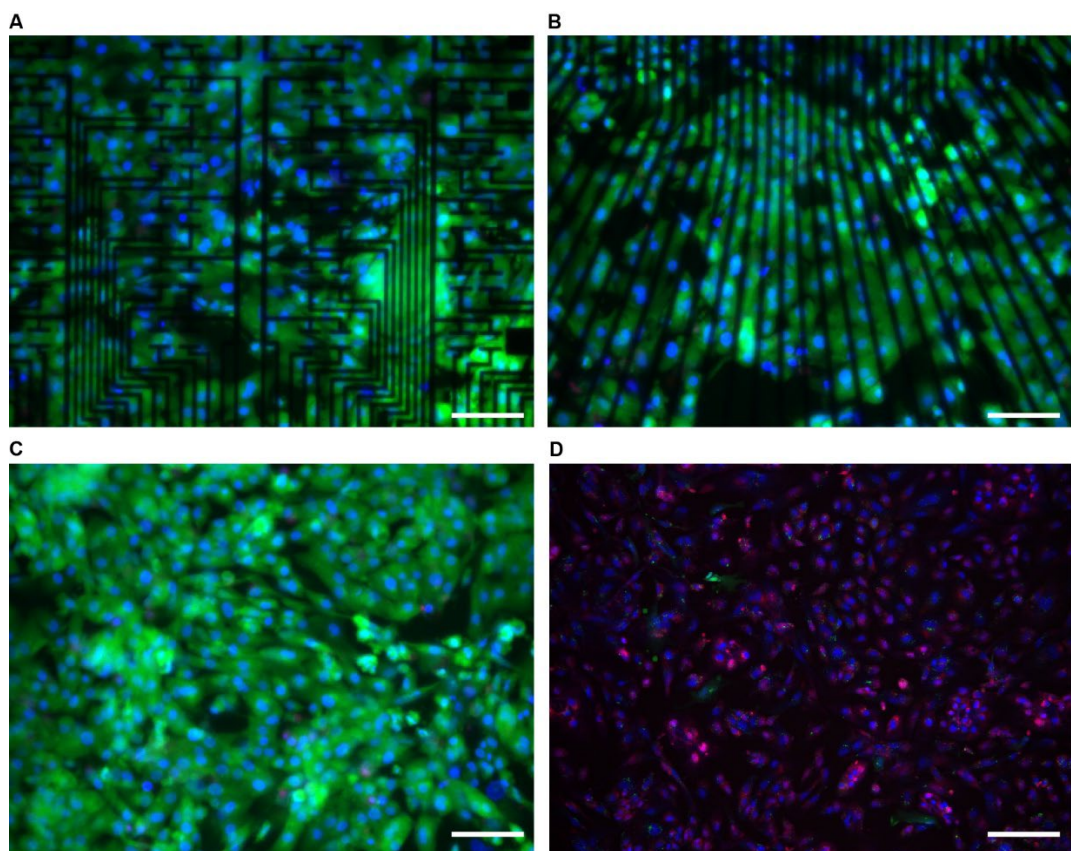
Fig. S6. Biocompatibility of integrated nanotransistor arrays revealed by cell viability assay. hESC-derived cardiomyocytes were cultured on the device substrate for 5 days before being stained with Hoechst 33342 (blue, nuclei), calcein-AM (green, live cells), and ethidium homodimer (red, dead cells). Optical imaging showed that >99% of the cardiomyocytes cultured on the nanotransistor (99.4±0.2%) (**A**) and interconnect (99.4±0.2%) (**B**) regions survived. The result showed no difference from cardiomyocytes cultured on a bare silica substrate (99.1±0.3%) (**C**). As negative control, cardiomyocytes treated with 100% ethanol (15 min) showed dominant dead state indicated by the red color (**D**). Three independent runs yield consistent results. Scale bars, 100 μm. Detailed procedure can be found in the *Materials and Methods* section.
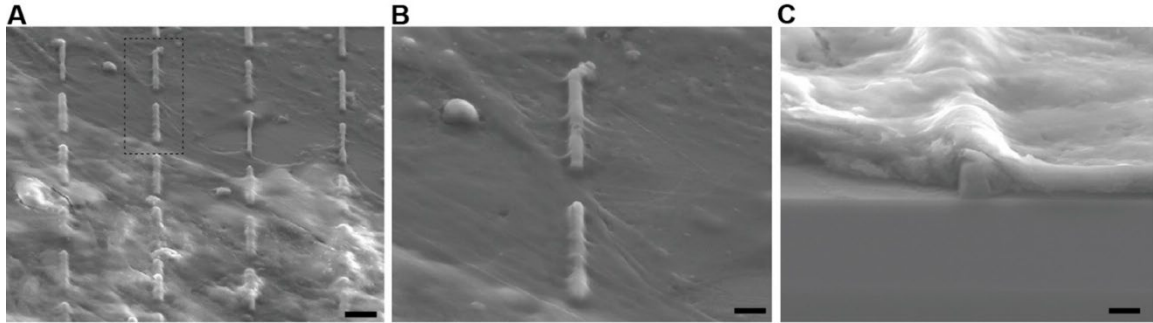
Fig. S7. Cell-device structure interface. Arrays of suspended nanowire structures were assembled and cultured with hESC-derived cardiomyocytes to study the cell-structure interface. Following standard procedure (*59*), the cardiomyocytes were fixed, dehydrated, treated with critical point drying to preserve the cell-structure interface before SEM imaging. (**A**) Perspective SEM image showing that the suspended Si nanowires were embedded in the monolayer of cardiomyocytes. Scale bar, 10 μm. (**B**) Zoom-in image (corresponding to dashed box in A) showing that the embedded Si nanowires still maintained the suspending structure without breakage. Scale bar, 3 μm. (**C**) Representative cross-sectional SEM image showing that the SU-8 microbar was conformally covered by the monolayer of cardiomyocytes. Scale bar, 1 μm. Detailed procedure can be found in the *Materials and Methods* section.
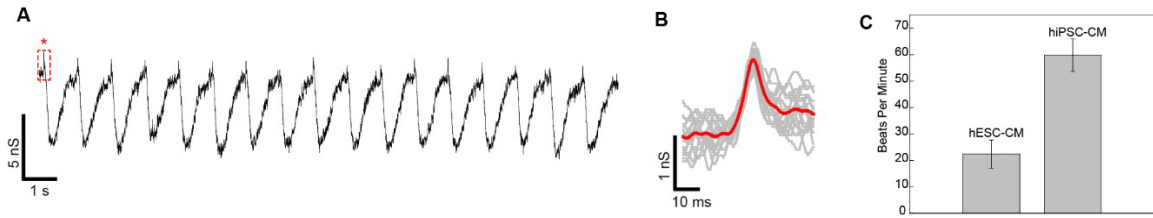
Fig. S8. Electrical recordings from hiPSC-CMs. (**A**) Representative recording showing periodic signal having the AP signal (marked by star) preceding a broad mechanical signal. (**B**) Superimposed AP signals. The red line represents the mean waveform. (**C**) Recorded contractile frequency in hiPSC-CMs (59.8 ± 6.1 beats per minute), compared to that in hESC-CMs (22.4 ± 5.3 beats per minute). The results were consistent with previous report (*62*).
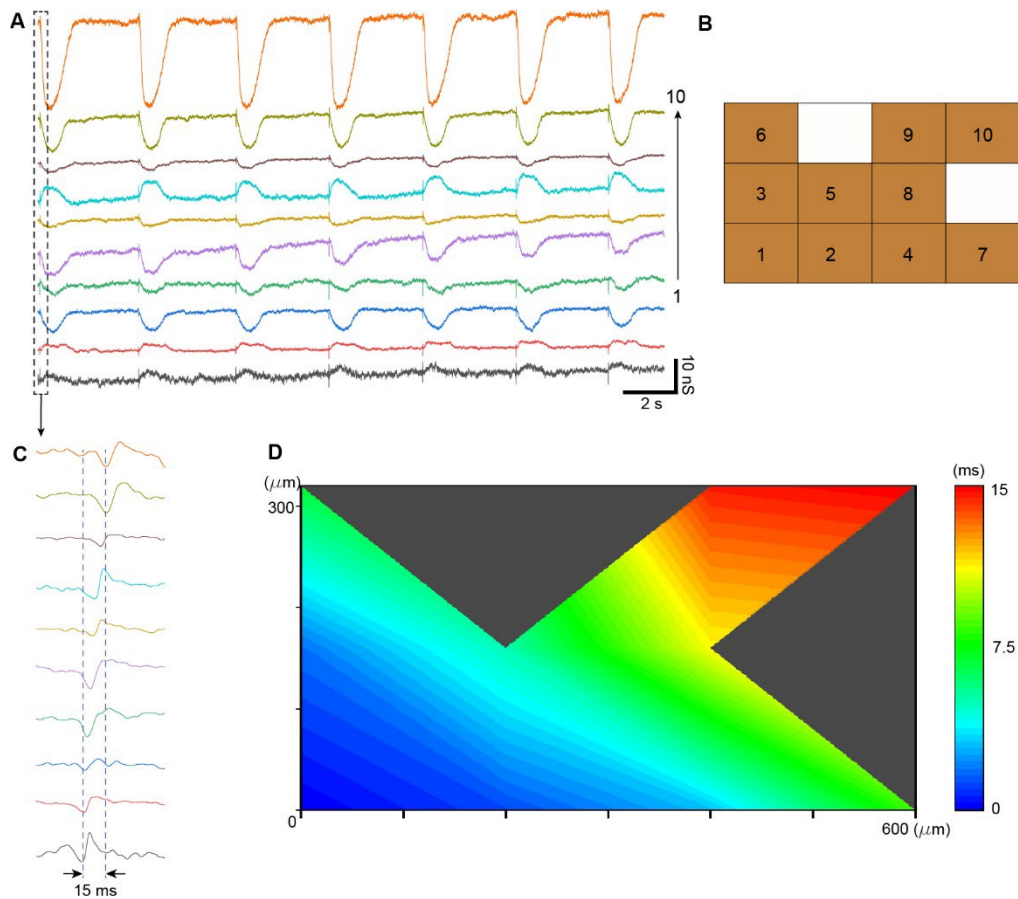
Fig. S9. 2D spatiotemporal mapping of electrical activity in hESC-CMs. (**A**) 10-channel recordings from cultured monolayered hESC-CMs. (**B**) The corresponding locations of the 10 devices (covering an area of 0.6×0.32 mm²). (**C**) Zoom-in action potentials (AP) from the dashed box region in (a). A time delay ~ 15 ms was revealed between devices 1 and 10, corresponding to an estimated velocity 4.5 cm/s consistent with reported values from *in vitro* hESC-CMs (*3*). The propagation was slower than that in *in vivo* neonatal myocardium (~20 cm/s), ventricles (~100 cm/s), and adult conduction systems (~300 cm/s), which was attributed to the immaturity in the *in vitro* cells (*63*). Note that immature phenotype is an intrinsic property in hESC-derived cardiomyocytes at the early stage (*64*). They are still considered promising *in vitro* models as they can retain genetic information from patient and continuous studies have been improving the maturity. (**D**) Computed contour map of signal propagation from (A, B). The two triangle regions correspond to two failed devices indicated in (B). Signal from device 1 (left bottom) was set as reference (*i.e.*, 0 s).
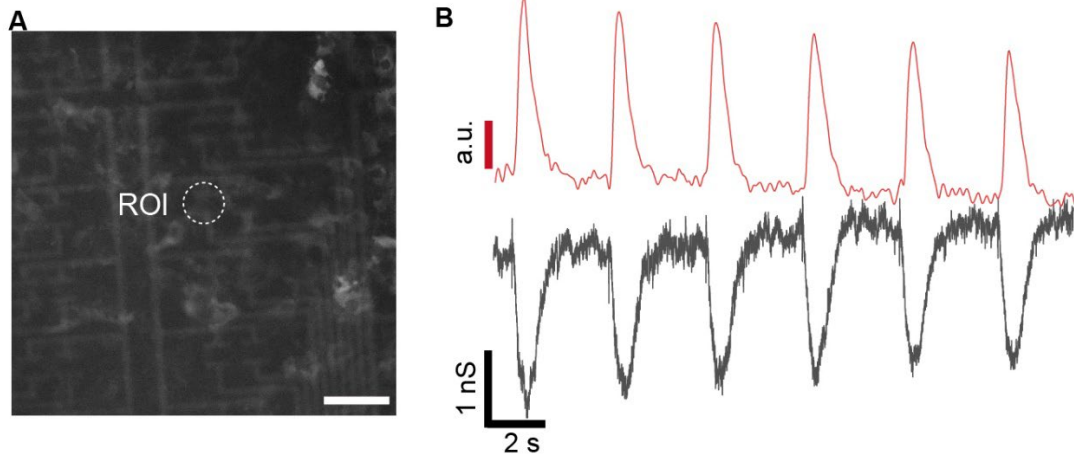
Fig. S10. Ca^{2+} imaging and electrical recording. (**A**) Imaging of the Ca^{2+} signal in the cardiomyocytes cultured on nanotransistor arrays. The circled region of interest (ROI) covers a nanotransistor. Scale bar, 100 μm. (**B**) Evolution of the intensity of Ca^{2+} signal in the ROI (upper) and correspondingly electrical signal recorded from the nanotransistor. Imaging details can be found in the *Materials and Methods* section.
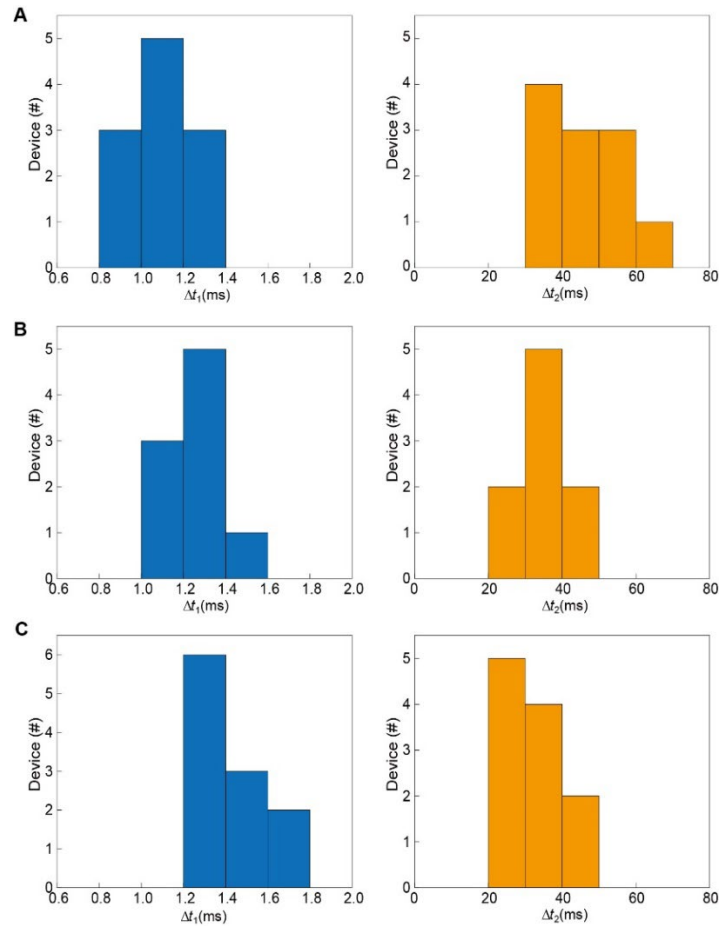
Fig. S11. Temporal dynamics in different cell cultures. Statistics of Δt_1 (width of the mechanical signal) and Δt_2 (time delay between AP and the initiation of the mechanical signal) in the main text (Figs. 2E, F) were collected from three batches of cell cultures. Statistics within each batch of cell culture can still yield batch-to-batch difference, with Δt_1, Δt_2 having values of (**A**) 1.08 ± 0.18 s, 44 ± 8 ms, (**B**) 1.24 ± 0.11 s, 34 ± 6 ms, and (**C**) 1.38 ± 0.14 s, 30 ± 7 ms in the three batches, respectively.

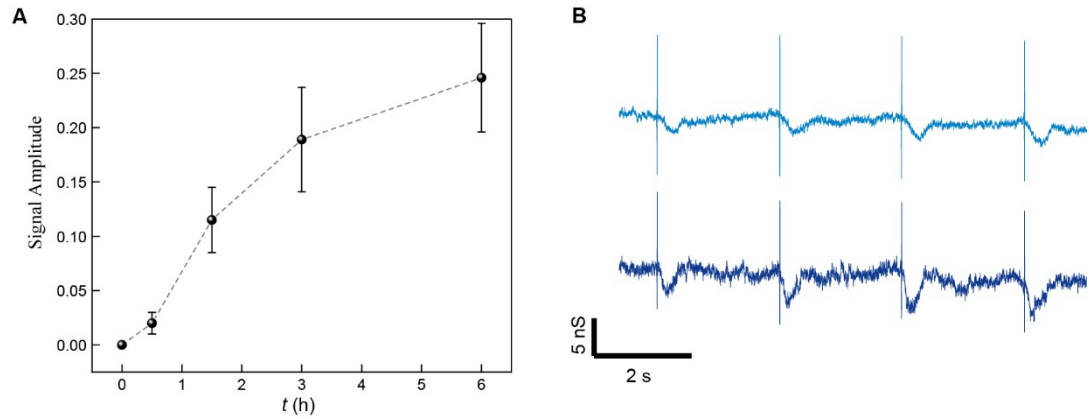**Fig. S12. Recovery of mechanical signal after washing out blebbistatin**. (**A**) The evolution of amplitude in recorded mechanical signals ($N = 6$) after washing out blebbistatin. The amplitude is normalized to the initial value before adding blebbistatin. The amplitude restored to ~25% value in 6 h. (**B**) Two representative recordings after washing out blebbistatin ($t = 6$ h).
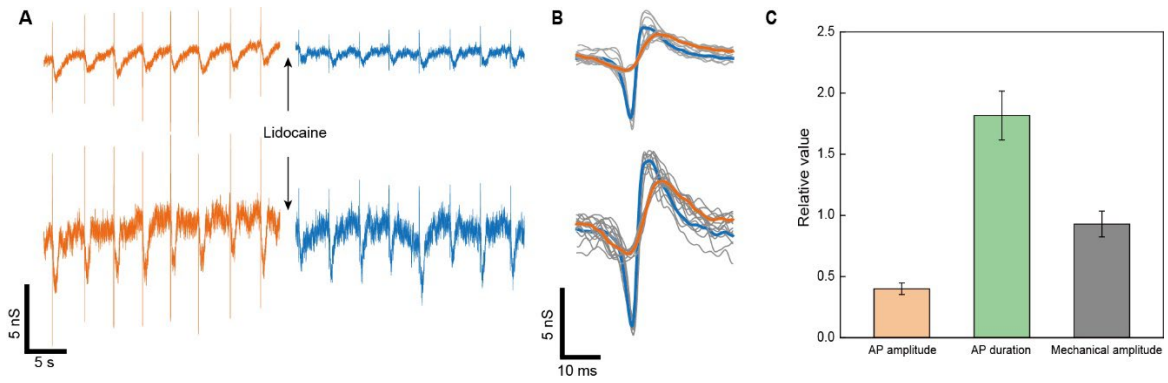
Fig. S13. Lidocaine effect detected by nanotransistors. (**A**) Recorded electrical signals from another two nanotransistors before (orange) and after (blue) adding lidocaine. (**B**) Superimposed AP signals before and after adding lidocaine, with the orange and blue curves representing the corresponding mean waveforms. (**C**) Average (N=3) relative values of AP amplitude (0.40 ± 0.05), AP duration (1.82 ± 0.20), and mechanical amplitude (0.93 ± 0.11) after adding lidocaine.
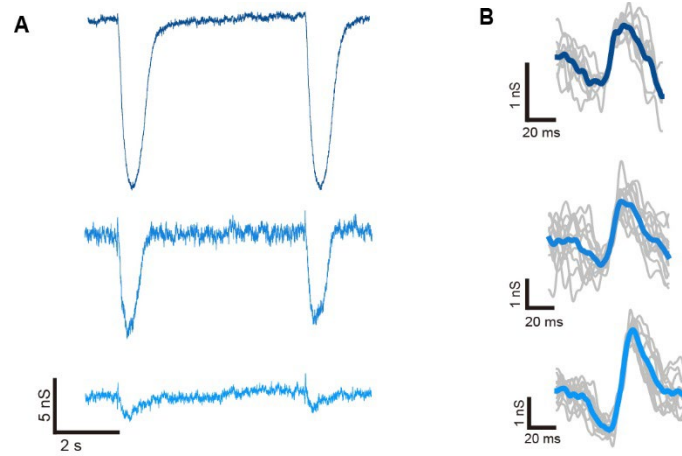
Fig. S14. Cell recovery by washing out isradipine. (**A**) Three representative recordings from hESC-CMs after being washed out isradipine ($t = 24$ h), showing the recovery of both mechanical and AP signals. (**B**) Corresponding superimposed AP signals from the recordings. The highlighted lines represent the mean waveforms.
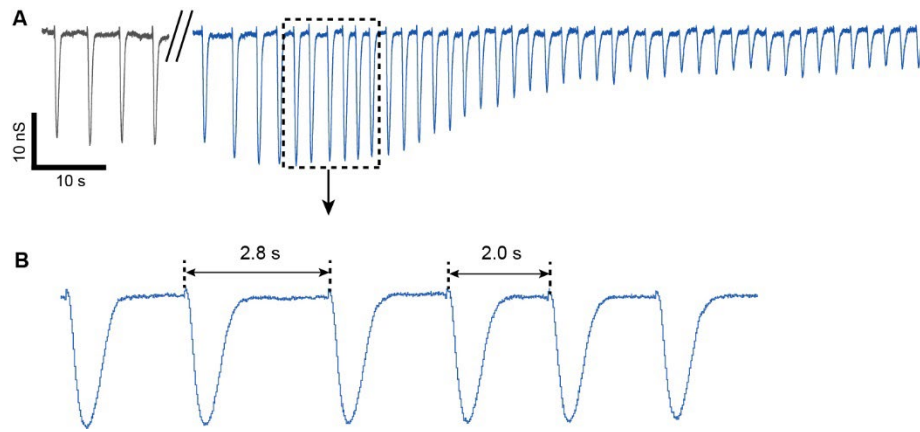
Fig. S15. K$^+$-blocker (E-4031) effect. (**A**) Electrical recroding from a sensor showing increased contractile frequency and fluctuation in amplitude after the treatment of E-4031 (50 nM). (**B**) Zoom-in signal also showing the fluctuation in contractile frequency. These traits were consistent with K$^+$-blocker induced arrhythmia behavior (*65*).
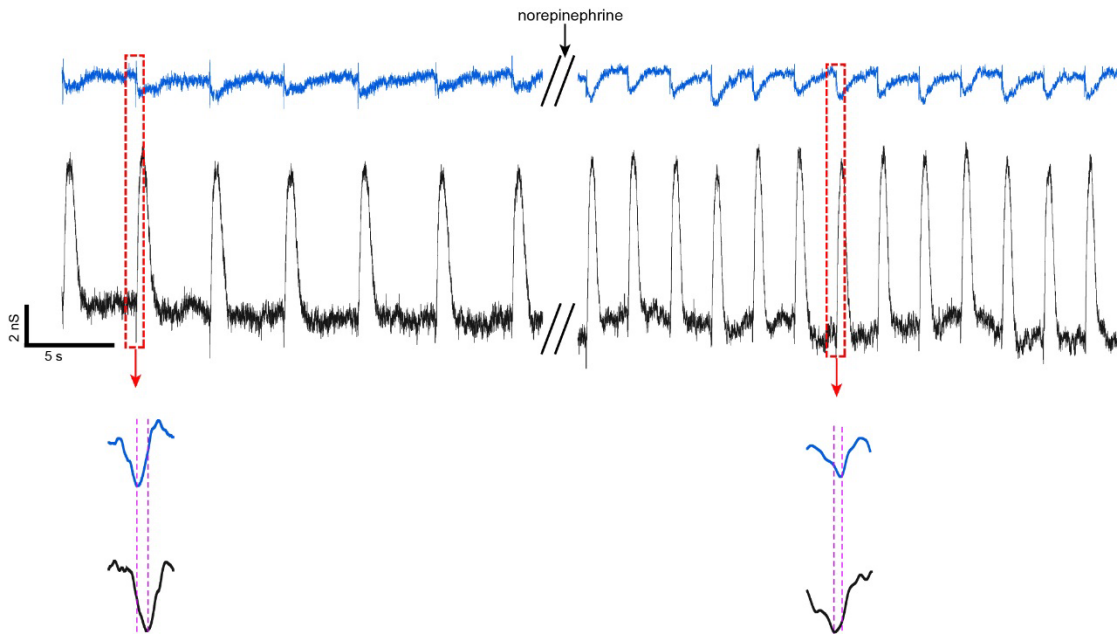
Fig. S16. Norepinephrine effect. Electrical recordings from two sensors before (left) and after (right) adding norepinephrine (10 µM). The contractile rate was observed to increase from 15 to 27 beats per minute. The zoon-in AP signals (bottom) showed a reverse in the conduction direction after the drug treatment. These behaviors were consistent with previous study (*11*).
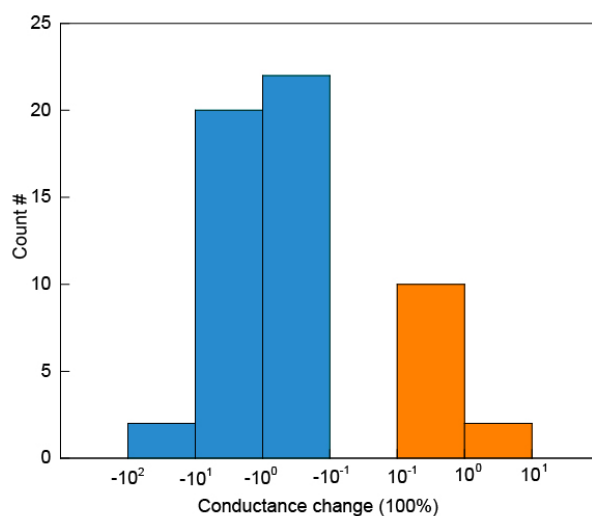
Fig. S17. Signal (sign & amplitude) distribution in recorded mechanical signals. Out of 60 devices, 44 (73.3%) showed negative signs or conductance decreases (blue columns) and 12 (20%) showed positive signs or conductance increases (orange columns). A small number of 4, (6.7%) showed mixed signs. The average conductance changes of the negative-sign and positive-sign signals were -1.67% (median value -0.9%) and 0.48% (median value 0.23%), respectively.

Fig. S18. Modeling of cell-sensor mechanical coupling. The cardiomyocyte was simulated by a $10\times10\times40$ μm^3 ($H\times W\times L$) box, with the contractile direction along the y-axis (L) and symmetric about the central plane $y=0$. For symmetry, it was assumed that the sensor was in the left half of the cell of $10\times10\t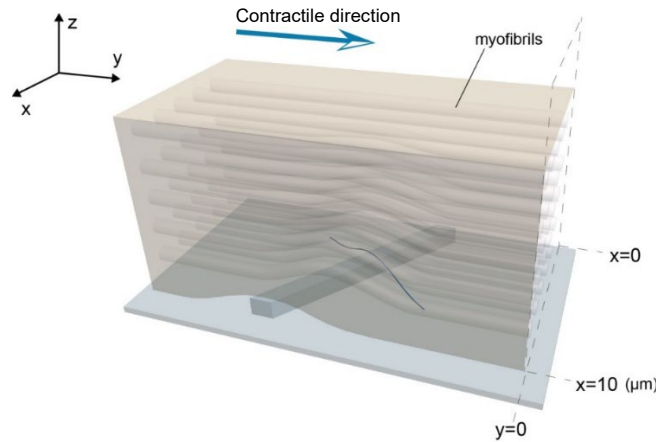imes20$ μm^3, with the boundary condition that the cell plane at $y=0$ could not move in y direction (but could slide in the x-z plane). At the extracellular interface, the cell model was excavated at the device region with the surface of the excavation following the geometry of the sensor, such that the sensor was in direct contact with cell surface (cell membrane). The cell consists of passive and contractile components as introduced previously (*66*). Linear elastic model was used for both components. To simulate the myofibril coverage in cardiomyocyte, the contractile component consists of 25 (5×5) cylindrical beam elements ($r = 0.5$ μm, $E = 67$ kPa) distributed along the cell totaling ~20% of the cell body, and the rest of the box (~80%) was filled with passive component ($E = 13.5$ kPa) (*67, 68*). Also, a Poisson's ratio of 0.48 (incompressible) was used for both components. The cell contraction was achieved through thermal contraction in the beam elements by reducing the temperature (*66*), which was to mimic sarcomere shortening caused by contraction in myofibrils. A contractile ratio of 5-15% in the beam elements was used (fig. S22), corresponding to typical value in cardiomyocytes shortening (*69*). Different contractile directions were obtained by rotating the sensor from 0° to 90° in increments of 15°. Finite-element mesh density of $0.1 - 1$ μm was used, with the convergence confirmed by a mesh refinement. As additional boundary conditions, no sliding was allowed at the bottom interface (cell-substrate and cell-nanowire interface). Also, the front and back surfaces of the cell ($x = 10$, $x = 0$) were allowed to slide in y-z plane but not in x direction (a frictionless-wall condition).

The displacements in the nodes of the curved section of nanowire were extracted and averaged by Abaqus to obtain the average nanowire displacement (fig. S19). For force, the maximal principal stress in the middle point of each element in curved section of nanowire was extracted. These values were averaged and multiplied by the cross-sectional area of the nanowire to obtain the average cellular force (fig. S22B).
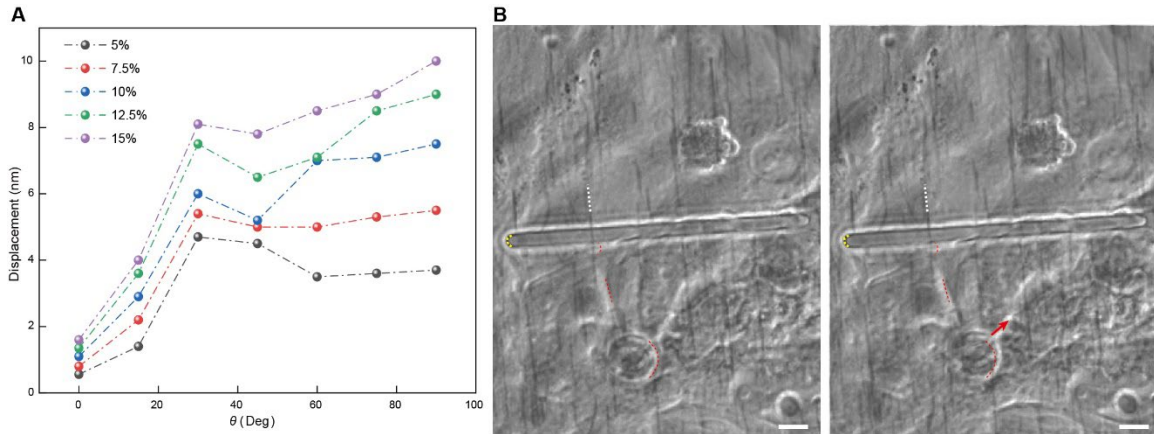
Fig. S19. Nanowire displacement at the cell-device interface. (**A**) The average displacement in the suspended nanowire during cell contraction with respect to the contractile direction (*i.e.*, interfacing angle θ) and contractile ratio (5-15%), revealed by mechanical simulation based on the model in fig. S18. (**B**) Optical images of the rest (left) and contraction (right) states in the monolayer of cardiomyocytes cultured on assembled suspended nanowire structures. By aligning to one terminal of the SU-8 microbar (yellow curve), the cells showed apparent movement (red dashed lines) toward direction indicated by the arrow, whereas the suspended nanowire (white dashed line) did not show observable movement. A better comparison can be made with video in movie S2. Scale bars, 2 μm.

Fig. S20. Image processing for cell-motion analysis (corresponding to Fig. 4c in main paper).
The vector of relative local displacement for each pixel in the nth frame ($\Delta x_{n,i,j}$, $\Delta y_{n,i,j}$) (i, j denoting the pixel indices) with respect to its previous neighboring $(n\text{-}1)^{th}$ frame was computed with Matlab (ver. R2021a; Mathworks) using Farneback method (*70*).

(**A**) Cumulative displacement for each pixel in the nth frame with respect to the 1st frame (cell resting state) computed by $x_{n,i,j} = \sum_{n=2}^{n} \Delta x_{n,i,j}$

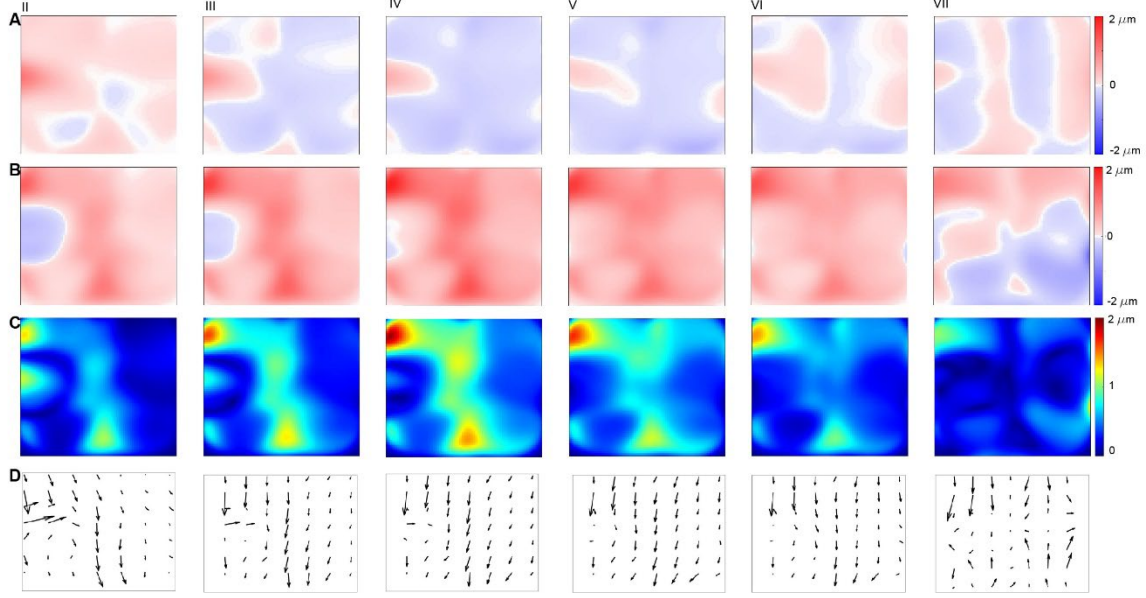(**B**) Cumulative displacement for each pixel in the nth frame with respect to the 1st frame computed by $y_{n,i,j} = \sum_{n=2}^{n} \Delta y_{n,i,j}$

(**C**) Amplitude of cumulative motion for each pixel computed by

$$D_{n,i,j} = \sqrt{x^2_{n,i,j} + y^2_{n,i,j}} = \sqrt{(\sum_{n=2}^{n} \Delta x_{n,i,j})^2 + (\sum_{n=2}^{n} \Delta y_{n,i,j})^2}$$

(**D**) Vector map of cumulative motion.

The angle θ_n of each vector in the nth frame computed by $\theta_n = atan(\frac{\sum_{n=2}^{n} \Delta y_{n,i,j}}{\sum_{n=2}^{n} \Delta x_{n,i,j}})$. The average angle $\overline{\theta}_n$ of the vectors in the nth frame, which characterizes the angle between cell contraction and the nanowire axis, was computed by:

$$\overline{\theta_n} = \frac{\sum_{i,j} D_{n,i,j} \times |tan^{-1}(y_{n,i,j}/x_{n,i,j}) - \phi|}{\sqrt{\sum_{i,j} D^2_{n,i,j}}},$$

where ϕ is the angle of nanowire axis with respect to the x axis. For symmetry, a range of $\overline{\theta}_n \leq 90°$ was considered. The pixel indices (i, j) cover the device region.
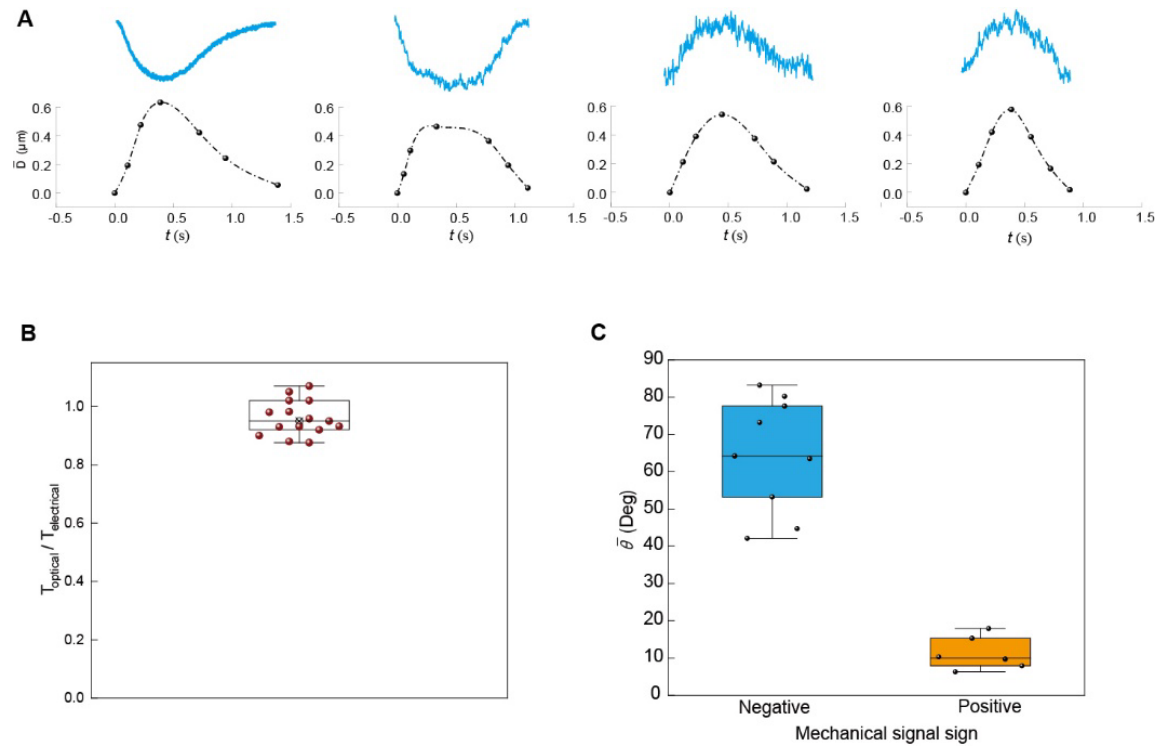
Fig. S21. Statistics (*N*=15) in electrical sensing signals from mechanical cellular response. (**A**) Additional representative electrical sensing signals (top) and optically tracked average amplitude ($\overline{D}$) of cellular motion at the device region. (**B**) Statistics of the comparison of the contractile time span between optical imaging (T_{optical}) and electrical recording ($T_{\text{electrical}}$). The results show that the electrical recordings from the nanotransistors can reliably track the contractile dynamics. (**C**) Statistics of the average $\overline{\theta}$ (*i.e.*, cell contractile direction with respect to nanowire axis) in different devices. The results showed a consistent trend that the electrical recordings showed negative signs for $\overline{\theta} > 25°$ and positive signs for $\overline{\theta} < 25°$.

Fig. S22. Predictive force measurement from electrically recorded signal. Mechanical information (*e.g.*, force) may be revealed from the electrically recorded signal, if a cell-nanowire interfacing angle θ is revealed by optical imaging. Note that this one-time optical registration can be still advantageous compared to full optical characterizations that require the continuous monitoring. The predictive force measurement is described as follows.

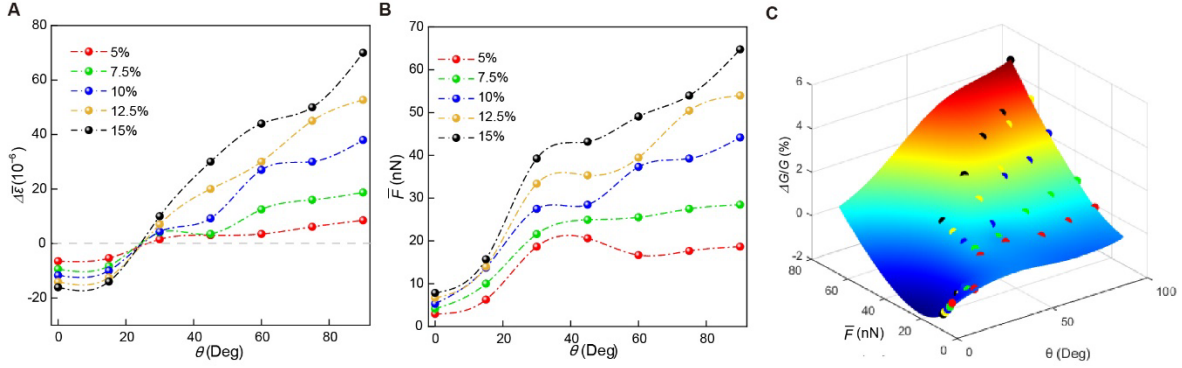(**A**) The net strain experience in the Si nanowire, $\overline{\Delta\varepsilon}$, is revealed by mechanical simulation under different cell contractile ratios (*e.g.*, 5-15%) and θ. The transition angle at which $\Delta\varepsilon$ changes sign is largely independent of the contractile ratio and has an average value of 25.0 ± 0.9°. The net strain can be readily related to the recorded electrical signal ($\Delta G/G$) as $\overline{\Delta\varepsilon} = (\Delta G/G)/g$, where g (gauge factor) has a revealed value of 7.6×10^2 (fig. S4). (**B**) The average force exerted on the Si nanowire, $\overline{F}$, can be also revealed by mechanical simulation under different contractile ratios and θ. Simulation details can be found in fig. S18. (**C**) With information in (A) and (B), we can establish a 3D fitting surface by using interpolation function griddata() in MATLAB, which can relate contractile ratio, $\overline{F}$, θ and sensing signal ($\Delta G/G$). For example, each measured value of $\Delta G/G$ and θ will define a curve on the fitting surface. The intersecting point of the two curves will find the corresponding $\overline{F}$ value and belonging of contractile ratio. Based on the fitting surface and the range of $\Delta G/G$ (0.1-10.5%) from electrical recordings (fig. S17), the estimated range of measured force is ~3-160 nN. The range is consistent with value of 0.1-144 nN revealed in previous study (*53*).
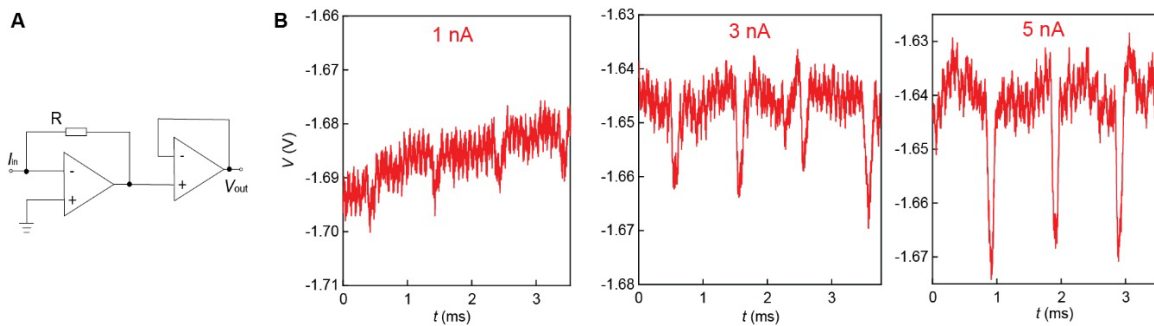
Fig. S23. Home-built current amplifier system. (**A**) Schematic of the amplifier system, which includes a first-stage current amplifier and a second-stage voltage follower to stabilize the signal. The amplified/converted signal is captured by a data acquisition system (Digidata 1440A). (**B**) Testing currents (100 μs width, 1 kHz) of 1 nA (left), 3 nA (middle), and 5 nA (right) were proportionally amplified to voltage signals. The performance in the amplifier ensures that it can capture the biosensing signal in the nA and kHz region.

Table S1. Comparison of field effect transistors used in cell/tissue interfaces.

Devices	Channel size (W×L)	Transconductance (Normalized transconductance)	Signal-to-noise ratio	Detected Signals	Ref.
Bottom-up planar Si nanowire	~0.03×2.3 μm^2	2.05 $\mu S \cdot V^{-1}$ (~70 $\mu S \cdot V^{-1} \cdot \mu m^{-1}$)	~3	Cardiomyocyte action potential	36
Top-down planar Si transistor	0.36×12 μm^2	4.5 ± 0.5 $\mu S \cdot V^{-1}$ (12.5 ± 1.4 $\mu S \cdot V^{-1} \cdot \mu m^{-1}$)	~7	Cardiomyocyte action potential	37
Bottom-up graphene transistor	60×60 μm^2	~2 $mS \cdot V^{-1}$ (~33 $\mu S \cdot V^{-1} \cdot \mu m^{-1}$)	~3-50	Neuron action potential	38
Bottom-up graphene transistor	20×10 μm^2	~4 $mS \cdot V^{-1}$ (~200 $\mu S \cdot V^{-1} \cdot \mu m^{-1}$)	~19	Cardiomyocyte action potential	39
PEDOT:PSS electrochemical transistor	~20×50 μm^2	12 $mS \cdot V^{-1}$ (~600 $\mu S \cdot V^{-1} \cdot \mu m^{-1}$)	3-7	Cardiomyocyte action potential	40
PEDOT:PSS electrochemical transistor	95×30 μm^2	~8 $mS \cdot V^{-1}$ (~84.2 $\mu S \cdot V^{-1} \cdot \mu m^{-1}$)	~18	Cardiomyocyte action potential	41
2,8-Difluoro-5,11-bis(triethylsilylethynyl)anthradithiophene organic transistor	2 cm×30 μm	~ 20 $\mu S \cdot V^{-1}$ (~1 $nS \cdot V^{-1} \cdot \mu m^{-1}$)	3-4	Cardiomyocyte action potential	42
3D Si nanotransistor	~0.03×20 μm^2	2.9 ± 0.7 $\mu S \cdot V^{-1}$ (97 ± 23 $\mu S \cdot V^{-1} \cdot \mu m^{-1}$)	3-8	Cardiomyocyte action potential + mechanical contraction	This work

Table S2. Comparison of piezoelectric sensors used in tissue interfaces.

Materials	Gauge factor	Device size	Force resolution	Ref.
Carbon composites	2.6	~4×8 mm^2	> 1 µN	30
Gold film	0.6	~3×5 cm^2	~70 nN	31
Si film	10-40	~20×20 µm^2	~0.1 nN	32
Cracked metal film	~100	~0.3×1 cm^2	~10 nN	33
Gold film	2.7	~0.4×0.5 mm^2	> 1 µN	34
3D Si nanotransistor	~760	~0.03×20 µm^2	~33 pN	This work

Other Supplementary Material for this manuscript includes the following:

Movie S1.
Synchronized contraction of monolayer cardiomyocytes cultured on the device.

Movie S2.
Displacement in the suspended Si nanowires interfaced with cardiomyocytes.

REFERENCES AND NOTES

1. D. M. Bers, Cardiac excitation-contraction coupling. *Nature* **415**, 198–205 (2002).

2. M. Clements, N. Thomas, High-throughput multi-parameter profiling of electrophysiological drug effects in human embryonic stem cell derived cardiomyocytes using multi-electrode arrays. *Toxicol. Sci.* **140**, 445–461 (2014).

3. D. Zhang, I. Y. Shadrin, J. Lam, H.-Q. Xian, H. R. Snodgrass, N. Bursac, Tissue-engineered cardiac patch for advanced functional maturation of human ESC-derived cardiomyocytes. *Biomaterials* **34**, 5813–5820 (2013).

4. J. I. Goldhabar, K. D. Philipson, Cardiac sodium-calcium exchange and efficient excitation-contraction coupling: Implications for heart disease. *Adv. Exp. Med. Biol.* **961**, 355–364 (2013).

5. B. J. van Meer, L. G. J. Tertoolen, C. L. Mummery, Concise review: Measuring physiological responses of human pluripotent stem cell derived cardiomyocytes to drugs and disease. *Stem Cells* **34**, 2008–2015 (2016).

6. N. Chopra, T. Yang, P. Asghari, E. D. Moore, S. Huke, B. Akin, R. A. Cattolica, C. F. Perez, T. Hlaing, B. E. Knollmann-Ritschel, Ablation of triadin causes loss of cardiac Ca^{2+} release units, impaired excitation–contraction coupling, and cardiac arrhythmias. *Proc. Natl. Acad. Sci.* **106**, 7636–7641 (2009).

7. J. D. Kijlstra, D. Hu, N. Mittal, E. Kausel, P. van der Meer, A. Garakani, I. J. Domian, Integrated analysis of contractile kinetics, force generation, and electrical activity in single human stem cell-derived cardiomyocytes. *Stem Cell Reports* **5**, 1226–1238 (2015).

8. M. Unal, Y. Alapan, H. Jia, A. G. Varga, K. Angelino, M. Aslan, I. Sayin, C. Han, Y. Jiang, Z. Zhang, Micro and nano-scale technologies for cell mechanics. *Nanobiomedicine* **1**, 5 (2014).

9. T. J. Herron, P. Lee, J. Jalife, Optical imaging of voltage and calcium in cardiac cells & tissues. *Circ. Res.* **110**, 609–623 (2012).

10. F. S. Alfonso, T. Zhou, E. Liu, A. F. McGuire, Y. Yang, H. Kantarci, D. Li, E. Copenhaver, J. B. Zuchero, H. Muller, B. Cui, Label-free optical detection of bioelectric potentials using electrochromic thin films. *Proc. Natl. Acad. Sci. U.S.A.* **117**, 17260–17268 (2020).

11. X. Dai, W. Zhou, T. Gao, J. Liu, C. M. Lieber, Three-dimensional mapping and regulation of action potential propagation in nanoelectronics-innervated tissues. *Nat. Nanotechnol.* **11**, 776–782 (2016).

12. M. E. Spira, A. Hai, Multi-electrode array technologies for neuroscience and cardiology. *Nat. Nanotechnol.* **8**, 83–94 (2013).

13. A. Zhang, C. M. Lieber, Nano-bioelectronics. *Chem. Rev.* **116**, 215–257 (2015).

14. B. Tian, J. Liu, T. Dvir, L. Jin, J. H. Tsui, Q. Qing, Z. Suo, R. Langer, D. S. Kohane, C. M. Lieber, Macroporous nanowire nanoelectronic scaffolds for synthetic tissues. *Nat. Mater.* **11**, 986–994 (2012).

15. Q. Li, K. Nan, P. Le Floch, Z. Lin, H. Sheng, T. S. Blum, J. Liu, Cyborg organoids: Implantation of nanoelectronics via organogenesis for tissue-wide electrophysiology. *Nano Lett.* **19**, 5781–5789 (2019).

16. J. Liu, T.-M. Fu, Z. Cheng, G. Hong, T. Zhou, L. Jin, M. Duvvuri, Z. Jiang, P. Kruskal, C. Xie, Z. Suo, Y. Fang, C. M. Lieber, Syringe-injectable electronics. *Nat. Nanotechnol.* **10**, 629–636 (2015).

17. A. Kalmykov, C. Huang, J. Bliley, D. Shiwarski, J. Tashman, A. Abdullah, K. Rastogi Sahil, S. Shukla, E. Mataev, W. Feinberg Adam, K. J. Hsia, T. Cohen-Karni, Organ-on-e-chip: Three-dimensional self-rolled biosensor array for electrical interrogations of human electrogenic spheroids. *Sci. Adv.* **5**, eaax0729 (2019).

18. G. Hong, C. M. Lieber, Novel electrode technologies for neural recordings. *Nat. Rev. Neurosci.* **20**, 330–345 (2019).

19. B. Desbiolles, M. M. Hannebelle, E. de Coulon, A. Bertsch, S. Rohr, G. Fantner, P. Renaud, Volcano-shaped scanning probe microscopy probe for combined force-electrogram recordings from excitable cells. *Nano Lett.* **20**, 4520–4529 (2020).

20. X. Zhang, L. Guo, H. Zeng, S. L. White, M. Furniss, B. Balasubramanian, E. Lis, A. Lagrutta, F. Sannajust, L. L. Zhao, B. Xi, X. Wang, M. Davis, Y. A. Abassi, Multi-parametric assessment of cardiomyocyte excitation-contraction coupling using impedance and field potential recording: A tool for cardiac safety assessment. *J. Pharmacol. Toxicol. Methods* **81**, 201–216 (2016).

21. F. Qian, C. Huang, Y.-D. Lin, A. N. Ivanovskaya, T. J. O'Hara, R. H. Booth, C. J. Creek, H. A. Enright, D. A. Soscia, A. M. Belle, R. Liao, F. C. Lightstone, K. S. Kulp, E. K. Wheeler, Simultaneous electrical recording of cardiac electrophysiology and contraction on chip. *Lab Chip* **17**, 1732–1739 (2017).

22. M. J. Berridge, The endoplasmic reticulum: A multifunctional signaling organelle. *Cell Calcium* **32**, 235–249 (2002).

23. D. E. Koser, A. J. Thompson, S. K. Foster, A. Dwivedy, E. K. Pillai, G. K. Sheridan, H. Svoboda, M. Viana, L. da F Costa, J. Guck, C. E. Holt, K. Franze, Mechanosensing is critical for axon growth in the developing brain. *Nat. Neurosci.* **19**, 1592–1598 (2016).

24. R. He, P. Yang, Giant piezoresistance effect in silicon nanowires. *Nat. Nanotechnol.* **1**, 42–46 (2006).

25. H. Gao, B. Yin, S. Wu, X. Liu, T. Fu, C. Zhang, J. Lin, J. Yao, Deterministic assembly of three-dimensional suspended nanowire structures. *Nano Lett.* **19**, 5647–5652 (2019).

26. J. K. Mouw, G. Ou, V. M. Weaver, Extracellular matrix assembly: A multiscale deconstruction. *Nat. Rev. Mol. Cell Biol.* **15**, 771–785 (2014).

27. Y. Zhu, F. Xu, Q. Qin, W. Y. Fung, W. Lu, Mechanical properties of vapor-liquid-solid synthesized silicon nanowires. *Nano Lett.* **9**, 3934–3939 (2009).

28. J. Yao, Y. Yan, C. M. Lieber, A nanoscale combing technique for the large-scale assembly of highly aligned nanowires. *Nat. Nanotechnol.* **8**, 329–335 (2013).

29. J. Yao, H. Yan, S. Das, J. F. Klemic, J. C. Ellenbogen, C. M. Lieber, Nanowire nanocomputer as a finite-state machine. *Proc. Natl. Acad. Sci. U.S.A.* **111**, 2431–2435 (2014).

30. T. A. Busbee, A. D. Valentine, F. S. Pasqualini, H. Yuan, M. Yadid, S.-J. Park, A. Kotikian, A. P. Nesmith, P. H. Campbell, J. J. Vlassak, J. A. Lewis, K. K. Parker, Instrumented cardiac microphysiological devices via multimaterial three-dimensional printing. *Nat. Mater.* **16**, 303–308 (2017).

31. J. U. Lind, M. Yadid, I. Perkins, B. B. O'Connor, F. Eweje, C. O. Chantre, M. A. Hemphill, H. Yuan, P. H. Campbell, J. J. Vlassak, K. K. Parker, Cardiac microphysiological devices with flexible thin-film sensors for higher-throughput drug screening. *Lab Chip* **17**, 3692–3703 (2017).

32. K. Matsudaira, T.-V. Nguyen, K. H. Shoji, T. Tsukagoshi, T. Takahata, I. Shimoyama, MEMS piezoresistive cantilever for the direct measurement of cardiomyocyte contractile force. *J. Micromech. Microeng.* **27**, 105005 (2017).

33. D.-S. Kim, Y. W. Choi, A. Shanmugasundaram, Y.-J. Jeong, J. Park, N.-E. Oyunbaatar, E.-S. Kim, M. Choi, D.-W. Lee, Highly durable crack sensor integrated with silicone rubber cantilever for measuring cardiac contractility. *Nat. Commun.* **11**, 535 (2020)

34. H. Zhao, Y. Kim, H. Wang, X. Ning, C. Xu, J. Suh, M. Han, J. Pagan-Diaz Gelson, W. Lu, H. Li, W. Bai, O. Aydin, Y. Park, J. Wang, Y. Yao, Y. He, M. T. A. Saif, Y. Huang, R. Bashir, J. A. Rogers, Compliant 3D frameworks instrumented with strain sensors for characterization of millimeter-scale engineered muscle tissues. *Proc. Natl. Acad. Sci. U.S.A.* **118**, e2100077118 (2021).

35. T. Cohen-Karni, B. P. Timko, L. E. Weiss, C. M. Lieber. Flexible electrical recording from cells using nanowire transistor arrays. *Proc. Natl. Acad. Sci. U.S.A.* **106**, 7309–7313 (2009).

36. T. Cohen-Karni, Q. Qing, Q. Li, Y. Fang, C. M. Lieber. Graphene and nanowire transistors for cellular interfaces and electrical recording. *Nano Lett.* **10**, 1098–1102 (2010).

37. J. F. Eschermann, R. Stockmann, M. Hueske, X. T. Vu, S. Ingebrandt, A. Offenhäusser, Action potentials of HL-1 cells recorded with silicon nanowire transistors. *Appl. Phys. Lett.* **95**, 083703 (2009).

38. A. B. Calia, E. Masvidal-Codina, T. M. Smith, N. Schafer, D. Rathore, E. Rodriguez-Lucas, X. Illa, J. M. Dela Cruz, E. D. Corro, E. Prats-Alfonso, D. Viana, J. Bousquet, C. Hebert, J. Martinez-Aguilar, J. R. Sperling, M. Drummond, A. Halder, D. Dodd, K. Barr, S. Savage, J. Fornell, J. Sort, C. Guger, R.

Villa, K. Kostarelos, R. C. Wykes, A. Guimera-Brunet, J. A. Garrido, Full-bandwidth electrophysiology of seizures and epileptiform activity enabled by flexible graphene microtransistor depth neural probes. *Nat. Nanotechnol.* **17**, 301–309 (2022).

39. B. M. Blaschke, M. Lottner, S. Drieschner, A. B. Calia, K. Stoiber, L. Rousseau, G. Lissourges, J. A. Garrido, Flexible graphene transistors for recording cell action potentials. *2D Mater.* **3**, 025007 (2016).

40. Y. Liang, M. Ernst, M. F. Brings, D. Kireev, V. Maybeck, A. Offenhäusser, D. Mayer, High performance flexible organic electrochemical transistors for monitoring cardiac action potential. *Adv. Healthc. Mater.* **7**, 1800304 (2018).

41. Y. Liang, F. Brings, V. Maybeck, S. Ingebrandt, B. Wolfrum, A. Pich, A. Offenhäusser, D. Mayer, Tuning channel architecture of interdigitated organic electrochemical transistors for recording the action potentials of electrogenic cells. *Adv. Funct. Mater.* **29**, 1902085 (2019).

42. A. Kyndiah, F. Leonardi, C. Tarantino, T. Cramer, R. Millan-Solsona, E. Garreta, N. Montserrat, M. Mas-Torrent, G. Gomila, Bioelectronic recordings of cardiomyocytes with accumulation mode electrolyte gated organic field effect transistors. *Biosens. Bioelectron.* **150**, 111844 (2020).

43. X. Duan, R. Gao, P. Xie, T. Cohen-Karni, Q. Qing, H. S. Choe, B. Tian, X. Jiang, C. M. Lieber, Intracellular recordings of action potentials by an extracellular nanoscale field-effect transistor. *Nat. Nanotechnol.* **7**, 174–179 (2012).

44. V. Vogel, M. Sheetz, Local force and geometry sensing regulate cell functions. *Nat. Rev. Mol. Cell Biol.* **7**, 265–275 (2006).

45. R. Parameswaran, K. Koehler, Y. Rotenberg Menahem, J. Burke Michael, J. Kim, K.-Y. Jeong, B. Hissa, D. Paul Michael, K. Moreno, N. Sarma, T. Hayes, E. Sudzilovsky, H.-G. Park, B. Tian, Optical stimulation of cardiac cells with a polymer-supported silicon nanowire matrix. *Proc. Natl. Acad. Sci. U.S.A.* **116**, 413–421 (2019).

46. N. Ballan, N. Shaheen, G. M. Keller, L. Gepstein, Single-cell mechanical analysis of human pluripotent stem cell-derived cardiomyocytes for drug testing and pathophysiological studies. *Stem Cell Reports* **15**, 587–596 (2020).

47. G. Q. Zhang, H. Wei, J. Lu, P. Wong, W. Shim, Identification and characterization of calcium sparks in cardiomyocytes derived from human induced pluripotent stem cells. *PLOS ONE* **8**, e55266 (2013).

48. S. Björk, E. A. Ojala, T. Nordström, A. Ahola, M. Liljeström, J. Hyttinen, E. Kankuri, E. Mervaala, Evaluation of optogenetic electrophysiology tools in human stem cell-derived cardiomyocytes. *Front. Physiol.* **8**, 884 (2017).

49. G. P. Farman, K. Tachampa, R. Mateja, O. Cazorla, A. Lacampagne, P. P. de Tombe, Blebbistatin: Use as inhibitor of muscle contraction. *Pflugers Arch.* **455**, 995–1005 (2008).

50. B. P. Bean, C. J. Cohen, R. W. Tsien, Lidocaine block of cardiac sodium channels. *J. Gen. Physiol.* **81**, 613–642 (1983).

51. H.-A. Lee, S.-A. Hyun, S.-G. Park, K.-S. Kim, S. J. Kim, Comparison of electrophysiological effects of calcium channel blockers on cardiac repolarization. *Korean J. Physiol. Pharmacol.* **20**, 119–127 (2016).

52. S. He, Y. Su, B. Ji, H. Gao, Some basic questions on mechanosensing in cell-substrate interaction. *J. Mech. Phys. Solids* **70**, 116–135 (2014).

53. M. L. Rodriguez, B. T. Graham, L. M. Pabon, S. J. Han, C. E. Murry, N. J. Sniadecki, Measuring the contractile forces of human induced pluripotent stem cell-derived cardiomyocytes with arrays of microposts. *J. Biomech. Eng.* **136**, 051005 (2014).

54. E. Karbassi, A. Fenix, S. Marchiano, N. Muraoka, K. Nakamura, X. Yang, C. E. Murry, Cardiomyocyte maturation: Advances in knowledge and implications for regenerative medicine. *Nat. Rev. Cardiol.* **17**, 341–359 (2020)

55. A. Chen, E. Lee, R. Tu, K. Santiago, A. Grosberg, C. Fowlkes, M. Khine, Integrated platform for functional monitoring of biomimetic heart sheets derived from human pluripotent stem cells. *Biomaterials* **35**, 675–683 (2014).

56. C. Bardy, M. van den Hurk, B. Kakaradov, J. A. Erwin, B. N. Jaeger, R. V. Hernandez, T. Eames, A. A. Paucar, M. Gorris, C. Marchand, R. Jappelli, J. Barron, A. K. Bryant, M. Kellogg, R. S. Lasken, B. P. F. Rutten, H. W. M. Steinbusch, G. W. Yeo, F. H. Gage, Predicting the functional states of human iPSC-

derived neurons with single-cell RNA-seq and electrophysiology. *Mol. Psychiatry* **21**, 1573–1588 (2016).

57. T. Kraft, J. Montag, A. Radocaj, B. Brenner, Hypertrophic cardiomyopathy: Cell-to-cell imbalance in gene expression and contraction force as trigger for disease phenotype development. *Circ. Res.* **119**, 992–995 (2016).

58. X. Lian, J. Zhang, S. M. Azarin, K. Zhu, L. B. Hazeltine, X. Bao, C. Hsiao, T. J. Kamp, S. P. Palecek, Directed cardiomyocyte differentiation from human pluripotent stem cells by modulating Wnt/β-catenin signaling under fully defined conditions. *Nat. Protoc.* **8**, 162–175 (2013).

59. R. Liu, J. Lee, Y. Tchoe, D. Pre, A. M. Bourhis, A. D'Antonio-Chronowska, G. Robin, S. H. Lee, Y. G. Ro, R. Vatsyayan, K. J. Tonsfeldt, L. A. Hossain, M. L. Phipps, J. Yoo, J. Nogan, J. S. Martinez, K. A. Frazer, A. G. Bang, S. A. Dayeh, Ultra-sharp nanowire arrays natively permeate, record, and stimulate intracellular activity in neuronal and cardiac networks. *Adv. Funct. Mater.* **32**, 2108378 (2022).

60. Z. Fan, J. C. Ho, Z. A. Jacobson, R. Yerushalmi, R. L. Alley, H. Razavi, A. Javey, Wafer-scale assembly of highly ordered semiconductor nanowire arrays by contact printing. *Nano Lett.* **8**, 20–25 (2008).

61. Z. Wang, A. A. Volinsky, N. D. Gallant, Crosslinking effect on polydimethylsiloxane elastic modulus measured by custom-built compression instrument. *J. Appl. Polym. Sci.* **131**, 41050 (2014).

62. Q. Zhao, X. Wang, S. Wang, Z. Song, J. Wang, J. Ma, Cardiotoxicity evaluation using human embryonic stem cells and induced pluripotent stem cell-derived cardiomyocytes. *Stem Cell Res Ther* **8**, 54 (2017).

63. M. R. Salick, B. N. Napiwocki, J. Sha, G. T. Knight, S. A. Chindhy, T. J. Kamp, R. S. Ashton, W. C. Crone, Micropattern width dependent sarcomere development in human ESC-derived cardiomyocytes. *Biomaterials* **35**, 4454–4464 (2014).

64. W. Zhang, C. W. Kong, M. H. Tong, W. H. Chooi, N. Huang, R. A. Li, B. P. Chan, Maturation of human embryonic stem cell-derived cardiomyocytes (hESC-CMs) in 3D collagen matrix: Effects of niche cell supplementation and mechanical stimulation. *Acta Biomater.* **49**, 204–217 (2017).

65. C. Follmer, T. Colatsky, Block of delayed rectifier potassium current, IK, by flecainide and E-4031 in cat ventricular myocytes. *Circulation* **82**, 289–293 (1990).

66. M. Nelson Celeste, P. Jean Ronald, L. Tan John, F. Liu Wendy, J. Sniadecki Nathan, A. Spector Alexander, S. Chen Christopher, Emergent patterns of growth controlled by multicellular form and mechanics. *Proc. Natl. Acad. Sci. U.S.A.* **102**, 11594–11599 (2005).

67. N. Weber, K. Schwanke, S. Greten, M. Wendland, B. Iorga, M. Fischer, C. Geers-Knörr, J. Hegermann, C. Wrede, J. Fiedler, H. Kempf, A. Franke, B. Piep, A. Pfanne, T. Thum, U. Martin, B. Brenner, R. Zweigerdt, T. Kraft, Stiff matrix induces switch to pure β-cardiac myosin heavy chain expression in human ESC-derived cardiomyocytes. *Basic Res. Cardiol.* **111**, 68 (2016).

68. J. S. Ribeiro Alexandre, Y.-S. Ang, J.-D. Fu, N. Rivas Renee, M. A. Mohamed Tamer, C. Higgs Gadryn, D. Srivastava, L. Pruitt Beth, Contractility of single cardiomyocytes differentiated from pluripotent stem cells depends on physiological shape and substrate stiffness. *Proc. Natl. Acad. Sci. U.S.A.* **112**, 12705–12710 (2015).

69. M. C. Ribeiro, R. H. Slaats, V. Schwach, J. M. Rivera-Arbelaez, L. G. J. Tertoolen, B. J. van Meer, R. Molenaar, C. L. Mummery, M. M. A. E. Claessens, R. Passier, A cardiomyocyte show of force: A fluorescent alpha-actinin reporter line sheds light on human cardiomyocyte contractility versus substrate stiffness. *J. Mol. Cell. Cardiol.* **141**, 54–64 (2020).

70. G. Farnebäck, in *Image Analysis*, J. Bigun, T. Gustavsson, Eds. (Springer Berlin Heidelberg, 2003), pp. 363–370.